Predictive capabilities of 2D and 3D block propagation models integrating block shape assessed from field experiments

Franck Bourrier, Vincent Acary

1 # Predictive capabilities of 2D and 3D block propagation
2 # models integrating block shape assessed from field
3 # experiments

4 **Franck Bourrier · Vincent Acary**

7 **Abstract** Block propagation models have been used for years for rockfall hazard
8 assessment. However, the calibration of model parameters that allow the simula-
9 tions to accurately predict rockfall trajectories for a given study site remains a key
10 issue.

11 This research aims at investigating the predictive capabilities of block propa-
12 gation models after a preliminary calibration phase. It is focused on models inte-
13 grating the shape of blocks since, despite their sound physical bases, they remain
14 less used than lumped-mass approaches due to their more recent popularisation.

15 Benefiting from both a recently built model integrating block shape, usable
16 in 2D and 3D, and from recent experimental results at the slope scale, we first
17 performed a calibration based on the use of the 2D model, and then we evaluated
18 the predictive capabilities of the calibrated model in 2D and in 3D using the
19 remaining part of the experimental results.

20 The calibrated model simulations predict the main characteristics of the propa-
21 gation, that is the preferential deposit zones and the ranges of velocities at specific
22 locations. Good matches between simulations and experimental results in both the
23 calibration and validation phases emphasizes the wide applicability of the model:
24 after a calibration phase on a sufficient number of different soil types, the model
25 may be used in a predictive manner. The good match between 2D and 3D simula-
26 tions also highlights the ease-of-use of the model for field applications, as the 2D

F. Bourrier
Univ. Grenoble Alpes, INRAE, ETNA, 38000 Grenoble, France
Univ. Grenoble Alpes, Inria, CNRS, Grenoble INP, Institute of Engineering, LJK, 38000,
Grenoble, France E-mail: franck.bourrier@inrae.fr

V. Acary
Univ. Grenoble Alpes, Inria, CNRS, Grenoble INP, Institute of Engineering, LJK, 38000,
Grenoble, France

model produces sufficiently accurate results while also being easier and faster to calibrate.

As classically observed for block propagation models, the model is not sufficient to predict the details of the velocity and stopping points but provides accurate predictions of the global ranges of these quantities, in particular of the extreme values. To lift these limitations in terms of predictive capabilities, more advanced calibration procedures based on optimization techniques constitute a promising path forward.

Keywords Rockfall · Model · Propagation · Fields experiments · Calibration

1 Introduction

Block propagation analysis is a key element in the process of rockfall hazard assessment. Although empirical approaches remain in use, block propagation is generally quantitatively analysed using process-based models (Volkwein et al., 2011). Among these, classical 2D lumped-mass models are still extensively used. They consider the block as a moving material point that propagates in interaction with the terrain, modelled as a 2D profile. Several levels of complexity exist regarding the modeling of the interaction between the block and the terrain, allowing models to account for the effects of both terrain and block properties (Dorren, 2003; Volkwein et al., 2011; Bourrier and Hungr, 2013). Despite the historical preeminence of 2D lumped-mass models, an increase in the use of more complex models has been observed for approximately twenty years. Several 3D lumped-mass models (e.g. Guzzetti et al., 2002; Dorren, 2003; Crosta and Agliardi, 2004; Lan et al., 2007) have been developed and are widely used. Models explicitly integrating block shape (e.g. Descoeudres and Zimmermann, 1987; Koo and Chern, 1998; Leine et al., 2014; Toe et al., 2018) have been more recently applied for practical case studies. Such models have existed for several decades (Falcetta, J.L., 1985; Descoeudres and Zimmermann, 1987), but their practical use has only been enabled by the recent increase in computational capabilities. The relatively recent interest in these models entails that the research results related to them (e.g. Toe et al., 2018; Lu et al., 2019, 2020; Garcia et al., 2020; Yan et al., 2020) are substantially less numerous than those related to lumped-mass models, in particular concerning their calibration and use in practice.

Although block propagation models have been used for years, the settings of the model parameters to guarantee the predictive capabilities of the simulations for a given study site remains difficult. As the number of existing rockfall events on the site of interest is usually very small, even sometimes nil, these settings cannot only be based on the comparison to these events. Most practitioners favor

settings based on the use of typical ranges of parameter values depending on the soil type, obtained from back analysis of simulations on several sites or given by the model developers. These values may be adjusted depending on the experience of the practitioner and on the observed deposited blocks and previous events on the site. Generally, the predictive capabilities of the simulations cannot directly be assessed, because of limited events on the site. Consequently, it relies on the quality of the block propagation model and of the associated calibration.

The calibration process complexity mainly depends on the characteristics of the propagation model. The use of models based on sound physical approaches simplifies the calibration process since such models are generally robust and involve parameters with clear physical meanings. The number of model parameters should also remain limited to its minimum because the assessment of the relative influence of the parameters is simplified and because it reduces the amount of data required for calibration. The questions of the amount of data required for a correct calibration and of the type of data required remain open. As mentioned above, the quantity of experimental data required for the calibration strongly depends on the robustness of the model and on the number of parameters. Both data at the rebound scale (Labiouse and Heidenreich, 2009; Bourrier et al., 2012; Asteriou and Tsiambaos, 2018; Lu et al., 2019) and at the slope scale (Giani et al., 2004; Dorren et al., 2006; Spadari et al., 2012; Hu et al., 2017; Volkwein et al., 2018; Caviezel et al., 2019; Williams et al., 2020) may be used. Finally, the calibration procedure should remain practically feasible. This question is crucial, especially for models that require large computational efforts, such as the propagation models explicitly integrating block shape.

The objective of this research work is twofold. We aim to: i) investigate the predictive capabilities of block propagation models that integrate the shape of blocks and ii) define a practice-oriented calibration procedure that requires moderate computational and field measurement effort. For that purpose, we made use of both a recently built model integrating block shape usable both in 2D and 3D and from recent experimental results at the slope scale.

The propagation model used is based on nonsmooth mechanics (Moreau, 1988; Brogliato, 2016), following recent research results in the field (Leine et al., 2014). The nonsmooth approach is a sound modeling framework to obtain a robust numerical method, which satisfies the threshold phenomena (friction, contact) and the dissipation properties of the model in discrete time, in particular impact dissipation and energy properties (Acary, 2015). In this article, the novel contribution is to include Coulomb-type rolling friction in addition to more standard phenomena such as frictional, plastic and impact dissipation processes at the interface between the soil and the block. Introducing rolling resistance to accurately model

the interaction was already shown to be efficient in (Bourrier et al., 2012; Garcia et al., 2020). The experimental dataset used in this article consists of data on two propagation paths with similar soil types. It provides sufficiently exhaustive, diversified, and detailed data to i) calibrate the model on the first path, and ii) assess its predictive capabilities on the second path. In addition, the extensive data related to block properties and trajectories on both sites, and the large number of blocks released, constitutes a substantial advantage for both the calibration and the assessment of predictive capabilities.

For the purpose of the study, we developed a practice-oriented calibration procedure. We first performed a calibration based on the use of the 2D model and of the experimental data on the first experimental path. Second, we evaluated the predictive capabilities of the calibrated model in 2D and in 3D using the remaining part of the experimental results. This works specifically investigates two key issues: i) the capacity of 2D models to reproduce block propagation trajectories calculated in 3D and ii) the existence of model parameters, associated with given soil types, suitable for both 2D and 3D models and for any site.

The field experiments and the modeling approach are respectively presented in Section 2 and Section 3. The results obtained are then detailed in Section 4, focusing first on the calibration of the model (Section 4.1) and, then, analysing the relevance and robustness of the simulation results (Section 4.2) as well as the predictive capabilities of the model (Section 4.3). Section 5 concludes the article with a detailed discussion of the results.

2 Field experiments

The field experiments used in this study for the calibration of the model and assessment of its predictive capabilities were collected with the objective of providing experimental data of block propagation for the assessment of various models predictive capacities for configurations where propagation simulations are potentially problematic (Bourrier et al., 2020).

The experiments, carried out in a quarry (Authume, France, owned by Pernot S.A), consisted in the successive release of more than one hundred blocks on two propagation paths. The first path, referred to as path A (Fig. 1), is characterized by an upper gentle slope section, made of newly deposited quarry waste, mixing sand, clay, and limestone fragments. This upper slope is overhanging a subvertical rock cut made of compact limestone rock and, at the toe of this wall, an horizontal track, made of compact quarry waste. A second rock cut, with the same characteristics as the first one, separates this track from the quasihorizontal platform, also made of compact quarry waste, acting as the terminal deposit area. The second

path, referred to as path B (Fig. 2), is characterized, in its upper section, by an inclined slope made of medium soft quarry waste, mixing sand, clay, and limestone fragments. This slope is bordered, at mid-distance, by a rock cut on one side and by a talus on the other, which creates a so-called corridor. The intermediate section of path B is characterized by two successive tracks, made of compact quarry waste, and separated by a short slope, made of medium soft quarry waste. The second track is followed by an inclined slope also made of medium soft quarry waste, terminated by a globally horizontal deposit area, made of compact quarry waste. For both paths, the altitude difference between the top and the bottom of the path is approximately $45m$.

The study site offers significant complexity and variability in terms of topography and surface characteristics. The combinations of gentle slopes and soft soils, involving block motion almost analogous to rolling, and the complex topographies with rapid changes in slope inclination and/or orientation favor challenging-to-model block trajectories. However, both the size of the propagation paths and the types of soils involved, in particular the soft soils made of quarry waste, are rather particular and obviously not representative for the variety of sites encountered when doing block propagation analyses.

A Digital Terrain Model (DTM - resolution: $0.2m$) was built in order to perform analyses of block trajectories. The DTM was generated from a set of images, taken from a UAV and from the ground. The images were treated using photogrammetry techniques (specifically the software Agisoft V1.2.6). A set of 20 control points covering the site, and located in a local coordinate system using a theodolite (Leica TS02), was used in the building process. Two GPS points and one geodesic point were also recorded to georeference the DTM.

Approximately fifty blocks were successively released on each propagation path using a power shovel. A release zone ($4m$ x $4m$ horizontal area) was delimited at the top of each path. The vertical release heights were set at $4m$ for path A and $2m$ for path B.

The blocks used in the experimental campaign were visually selected to obtain block volumes approximately ranging between 0.1 and $0.75m^3$. The range of block volumes is rather restricted compared to the wide range potentially encountered in rockfall events. Consequently, the block-terrain interactions observed in the experiments are potentially not representative for all the processes involved in block propagation.

Each block was weighed and three principal lengths (L_1, L_2, and L_3, with $L_1 > L_2 > L_3$) were measured for each block. These lengths characterize the minimal parallelepiped that incorporates the block. No additional measurements

of block shapes, such as their reconstruction using photogrammetry for example, have been made during the experimental campaign.

The quantitative analysis of block kinematics focused on measurements at specific locations of the site, called *Evaluation Screens (ES)* (Figures 1 and 2), using cameras with shooting range focused on the *ES*. For path A, the first evaluation screen ($ES1 - A$) was located at the end of the uphill gentle slope, just before the first rock cut, and the second one ($ES2 - A$) at the top of the downhill rock cut. For path B, $ES1 - B$ is the contour line at the elevation of the corridor beginning while $ES2 - B$ was located at the downstream extremity of the first sloping track.

The blocks velocities were measured at the *ES*. For these measurements, two positions of the block at the slope surface before and after the *ES* and the duration taken by the block to travel this distance were first measured from projections of the video footage images on the DTM of the site. Second, the velocity at the *ES* was calculated assuming either free flight or rolling of the block. In the first case, the block positions just before and just after the evaluation screen correspond to successive impact points and the velocity at the *ES* was calculated assuming a parabolic trajectory of the block. Details of this calculation can be found in Bourrier et al. (2012). In the second one, the velocity at the evaluation screen was assimilated to the mean velocity between the two positions. The error in terms of velocity measurement is mainly due to errors on the visual positioning of the points on the DTM. This error is estimated around $0.5m$, inducing errors on the velocity around $1m/s$.

Complementary, precise determination of the blocks' stopping points locations were conducted after each series of five blocks released. The theodolite used for this purpose (Leica TS02) provided measurements with an estimated accuracy of $0.1m$, mainly resulting from uncertainties associated with the visual assessment of blocks' centers of gravity. In the case of breakage of the block, the stopping point considered was the stopping point of the largest resulting fragment, if it could be identified, or the last impact point before breakage, if the block broke into several small pieces.

Further details about the study site, the experimental protocol, and the measurements can be found in Bourrier et al. (2020).

As the experimental dataset consists of data on two propagation paths with similar soil types, it is very well adapted for, firstly, calibrating a propagation model on one path and, secondly, assessing the predictive capabilities of the model on the second one. In addition, the number of different types of soils remains limited (medium compacted quarry waste, compacted quarry waste, and compact rock), which simplifies the calibration phase, and the type of soils are similar on both paths, which is crucial for a calibration on one path, followed by an

assessment of predictive capabilities on the second one. Finally, the extensive data related to block properties and trajectories on both sites and the large number of blocks released constitutes a substantial advantage for both the calibration and the assessment of predictive capabilities.

3 Block propagation modeling

3.1 Propagation model description

The propagation model was developed using the Siconos software (Acary et al., 2019)[1]. Siconos is an open-source scientific software primarily targeted at modeling and simulating nonsmooth dynamical systems.

The propagation model allows the simulation of the 3D propagation of a block modelled as a convex facetized rigid body interacting with a terrain, modelled as a triangulated surface. In 2D, the block is a polygon, and the surface a polyline. As classically done in block propagation models, successive releases of blocks with different initial conditions are simulated to quantify the variability of the block propagation process. For each block, the propagation modeling is a time-stepping process. At each time step, the occurrence of an interaction between the block and the surface is checked. In the case of an interaction, an impulse is applied to the block. The propagation stops when the block reaches its static equilibrium.

3.1.1 Propagation of a block

In a three-dimensional configuration, the position of the block center of mass is denoted $x_{\mathsf{g}} \in I\!\!R^3$, and the block orientation is characterized by the rotation matrix $\mathbf{R} \in I\!\!R^{3\times3}$ of the body-fixed frame with respect to a given inertial frame. The rotation matrix is parametrized by a unit quaternion $\mathsf{q} \in I\!\!R^4$, $\|\mathsf{q}\| = 1$ such that $\mathbf{R} = \varPhi(\mathsf{q})$, $\dot{\mathsf{q}} = \varPsi(\mathsf{q})\varOmega$ where $\varOmega \in I\!\!R^3$ is the angular velocity of the body expressed in the body–fixed frame. Formulae for $\varPhi$ and $\varPsi$ can be found in standard textbooks on multi-body dynamics (Géradin and Cardona, 2001). We denote by q the generalized coordinate vector of the block, and by v the associated generalized velocity vector:

$$q := \begin{bmatrix} x_{\mathsf{g}} \\ \mathsf{q} \end{bmatrix}, \quad v := \begin{bmatrix} v_{\mathsf{g}} \\ \varOmega \end{bmatrix}. \tag{1}$$

The relation between v and the time derivative of q is

$$\dot{q} = \begin{bmatrix} \dot{x}_{\mathsf{g}} \\ \varPsi(\mathsf{q})\dot{\mathsf{q}} \end{bmatrix} = \begin{bmatrix} I_3 & 0 \\ 0 & \varPsi(\mathsf{q}) \end{bmatrix} v := T(q)v \tag{2}$$

---

[1] http://github.com/siconos/siconos

with $T(q) \in I\!\!R^{7\times 6}$, and I_3 the identity matrix. Note that the generalized velocity vector v is not directly the time derivative of the generalized coordinate vector.

The Newton-Euler equation in compact form may be written as:

$$\begin{cases} \dot{q} = T(q)v, \\ M\dot{v} = F(q,v) \end{cases} \tag{3}$$

$M \in I\!\!R^{6\times 6}$ is the total inertia matrix

$$M := \begin{pmatrix} mI_3 & 0 \\ 0 & I \end{pmatrix}, \tag{4}$$

where $m > 0$ is the mass, $I \in I\!\!R^{3\times 3}$ is the matrix of moments of inertia around the center of mass and the axis of the body–fixed frame.

The vector $F(q,v) \in I\!\!R^6$ collects all the forces and torques applied to the body

$$F(q,v) := \begin{pmatrix} f(x_{\mathsf{g}}, v_{\mathsf{g}}, \mathsf{q}, \Omega) \\ I\Omega \times \Omega + t(x_{\mathsf{g}}, v_{\mathsf{g}}, \mathsf{q}, \Omega) \end{pmatrix}. \tag{5}$$

where the vectors $f(\cdot) \in I\!\!R^3$ and $t(\cdot) \in I\!\!R^3$ are the total forces and torques applied to the body, respectively. The term $I\Omega \times \Omega$ represents the gyroscopic forces.

Among the other forces and torques applied to the body, those induced by the contact between the slope surface and the block are essential. In the model, these forces are considered as unilateral constraints applied to the block. The distance between the block and the surface is associated with a gap function $g(q)$ and the block is subjected to the unilateral constraint $g(q) \geq 0$, that prevents the penetration of the block into the ground. The unilateral constraint generates a generalized reaction force applied to the body defined by $R \in I\!\!R^6$.

The value of R is characterized using an impact law that governs the interaction between the block and the slope surface. Impact laws are classically expressed in local contact frames. For that reason, the local relative velocity u and the local reaction p are expressed in terms of generalized variables with linear relations for a given q as:

$$\begin{aligned} u &= G^\top(q)v \\ R &= G(q)p. \end{aligned} \tag{6}$$

where $G^\top(q)$ is the operator relating local variables to global ones.

In the simple case of m frictionless unilateral constraints, the Newton-Euler equations can thus be written as:

$$\begin{cases} \dot{q} = T(q)v, \\ M\dot{v} = F(q,v) + R \\ u = G^{\top}(q)v, \quad R = G(q)p \\ 0 \ \leq \ g(q) \perp p \ \geq \ 0. \end{cases} \tag{7}$$

where $u \in \mathbb{R}^m, p \in \mathbb{R}^m$ and $G(q) \in \mathbb{R}^{6 \times m}$. The inequalities involving vectors are understood to hold component-wise and the $x \perp y$ symbol means that $y^{\top}x = 0$. The last line of (7) is the contact law, also known as the Signorini condition.

A specific impact law involving Coulomb friction with rolling resistance at the contact was implemented in the model. This law involves a standard Coulomb friction law which is a set-valued force law that generates a resistive force to sliding, *i.e.* opposite to the sliding velocity. The Coulomb-type rolling friction law, considered in this article, is also a set-valued force law that generates a resistive moment to rolling, *i.e.* opposite to the rolling velocity. This rolling friction model has been developed in Acary and Bourrier (2021) and only the main features are recalled in a three-dimensional setting, but the following formulation can be easily specified for a 2D configuration.

As mentioned previously, the formulation of the impact law requires the definition of local variables at contact. Let us assume that we can uniquely define an orthonormal contact frame at the contact point C denoted by $(C, \mathsf{N}, \mathsf{T}_1, \mathsf{T}_2)$, where $\mathsf{N} \in \mathbb{R}^3$ defines an outward unit normal vector to the block at point C and $\mathsf{T}_1 \in \mathbb{R}^3, \mathsf{T}_2 \in \mathbb{R}^3$ are unit tangent vectors. The reaction force exerted by the block on the surface is denoted by $r \in \mathbb{R}^3$. It can be decomposed in the contact frame as

$$r := r_{\mathrm{N}}\mathsf{N} + r_{\mathrm{T}_1}\mathsf{T}_1 + r_{\mathrm{T}_2}\mathsf{T}_2, \quad \text{with } r_{\mathrm{N}} \in \mathbb{R} \text{ and } r_{\mathrm{T}} := [r_{\mathrm{T}_1}, r_{\mathrm{T}_2}]^{\top} \in \mathbb{R}^2, \tag{8}$$

where r_{T} is the tangent reaction, that will be used to model Coulomb friction. The relative velocity at contact $u \in \mathbb{R}^3$ is used as natural way to formulate friction. It is also decomposed as

$$u := u_{\mathrm{N}}\mathsf{N} + u_{\mathrm{T}_1}\mathsf{T}_1 + u_{\mathrm{T}_2}\mathsf{T}_2 \quad \text{with } u_{\mathrm{N}} \in \mathbb{R} \text{ and } u_{\mathrm{T}} = [u_{\mathrm{T}_1}, u_{\mathrm{T}_2}]^{\top} \in \mathbb{R}^2, \tag{9}$$

where u_{T} is the sliding relative local velocity. In order to formulate the Coulomb-type rolling friction at contact, we also introduce the relative angular velocity $\omega_{\mathrm{R}} \in \mathbb{R}^2$ and the rolling friction reaction torque $m_{\mathrm{R}} \in \mathbb{R}^2$ at contact. To obtain a compact formulation of the impact model, we denote the local variables at contact

by:

$$p := \begin{bmatrix} r_{\mathrm{N}} \\ r_{\mathrm{T}} \\ m_{\mathrm{R}} \end{bmatrix} = \begin{bmatrix} r \\ m_{\mathrm{R}} \end{bmatrix} \text{ and } y := \begin{bmatrix} u_{\mathrm{N}} \\ u_{\mathrm{T}} \\ \omega_{\mathrm{R}} \end{bmatrix} = \begin{bmatrix} u \\ \omega_{\mathrm{R}} \end{bmatrix}. \tag{10}$$

At the velocity level, the Signorini condition is written

$$\begin{cases} 0 \leq u_{\mathrm{N}} \perp r_{\mathrm{N}} \geq 0 & \text{if } g(q) \leq 0 \\ r_{\mathrm{N}} = 0 & \text{otherwise.} \end{cases} \tag{11}$$

The motion of the block is expected to be nonsmooth since impacts occur when the block hits the ground. The model must be completed by an impact law that will define the post-impact velocity u_{N}^{+} with respect to, at least, the pre-impact velocity u_{N}^{-}. The simplest choice is to use the Newton impact law that can be written as

$$u_{\mathrm{N}}^{+} = -e_c u_{\mathrm{N}}^{-}, \tag{12}$$

where $e_c \geq 0$ is the coefficient of restitution. If impact occurs, the reaction p, and its components, r and m_{R} are no longer homogeneous to forces but to impulses. As is usually done in impact mechanics (Moreau, 1988; Brogliato, 2016), the contact law with unilateral constraints and friction is written in terms of local relative velocities and impulses. The Newton impact law can be included in the complementary condition at the velocity level as

$$0 \leq \bar{u}_{\mathrm{N}} \perp r_{\mathrm{N}} \geq 0 \text{ if } g(q) \leq 0, \tag{13}$$

with $\bar{u}_{\mathrm{N}} := u_{\mathrm{N}}^{+} + e_c u_{\mathrm{N}}^{-}$ and r_{N} is the normal reaction impulse. For $g(q) > 0$, we trivially have $p = 0$. For $g(q) \leq 0$, the Coulomb friction model with unilateral contact and rolling resistance is defined in all modes, following the work in Acary and Bourrier (2021):

− take–off:
$$p = 0, \bar{u}_{\mathrm{N}} \geq 0, \tag{14}$$

− sticking and no-rolling:
$$p \in K_r, u = 0, \omega_{\mathrm{R}} = 0, \tag{15}$$

− sliding and no-rolling:

$$p \in K_r, \bar{u}_{\mathrm{N}} = 0, \|r_{\mathrm{T}}\| = \mu_c r_{\mathrm{N}}, \|m_{\mathrm{R}}\| < \mu_{r,c} r_{\mathrm{N}}, \|r_{\mathrm{T}}\| u_{\mathrm{T}} = -\|u_{\mathrm{T}}\| r_{\mathrm{T}}, \omega_{\mathrm{R}} = 0, \tag{16}$$

– sticking and rolling:

$$p \in K_r, \bar{u}_{\mathrm{N}} = 0, \|r_{\mathrm{T}}\| < \mu_c r_{\mathrm{N}}, \|m_{\mathrm{R}}\| = \mu_{r,c} r_{\mathrm{N}}, \|m_{\mathrm{R}}\|\omega_{\mathrm{R}} = -\|\omega_{\mathrm{R}}\|m_{\mathrm{R}}, u_{\mathrm{T}} = 0, \tag{17}$$

– and sliding and rolling:

$$p \in \partial K_r, \bar{u}_{\mathrm{N}} = 0, \|r_{\mathrm{T}}\| = \mu_c r_{\mathrm{N}}, \|m_{\mathrm{R}}\| = \mu_{r,c} r_{\mathrm{N}},$$
$$\|r_{\mathrm{T}}\|u_{\mathrm{T}} = -\|u_{\mathrm{T}}\|r_{\mathrm{T}}, \quad \|m_{\mathrm{R}}\|\omega_{\mathrm{R}} = -\|\omega_{\mathrm{R}}\|m_{\mathrm{R}}, \tag{18}$$

where the extended friction cone K_r is defined as the cone of admissible reaction forces and torques, by

$$K_r = \{p \in I\!\!R^5 \mid \|r_{\mathrm{T}}\| \le \mu r_{\mathrm{N}}, \quad \|m_{\mathrm{R}}\| \le \mu_{r,c} r_{\mathrm{N}}\} \subset I\!\!R^5, \tag{19}$$

and its boundary is given by

$$\partial K_r = \{p \in I\!\!R^5 \mid \|r_{\mathrm{T}}\| = \mu r_{\mathrm{N}}, \quad \|m_{\mathrm{R}}\| = \mu_{r,c} r_{\mathrm{N}}\} \subset I\!\!R^5. \tag{20}$$

Although the model of the interaction between the block and the soil does not allow the soil deformation to be explicitly accounted for during impact, it integrates block energy losses due to plasticity, viscosity and wave propagation by means of the restitution coefficient e_c. The frictional processes at the interface are also accounted for using μ_c. Finally, the rolling friction coefficient $\mu_{r,c}$ quantifies cratering and resistance of the soil to block rolling around the contact point.

Some details on the numerical implementation of the complete rolling friction model can be found in Acary and Bourrier (2021). In this work, the simulations have been done with the Moreau-Jean time-stepping scheme (Jean and Moreau, 1987; Acary and Brogliato, 2008) based on a θ-method for the smooth terms and the projected Gauss-Seidel method for the discrete frictional contact problems (Jourdan et al., 1998; Acary et al., 2018). The numerical methods are implemented in the Siconos software (available as a free open-source software) and the version v4.3.0 is used in this article.

The θ parameter is set equal to 1/2 to avoid the numerical dissipation of energy due to the time-stepping scheme (Acary, 2015). The time step and the error tolerance of the projected Gauss-Seidel solver are set at $10^{-3}s$ and 10^{-4}, respectively. Under these simulation conditions, the computational effort to compute the propagation of 50 blocks on path A or B is typically a few minutes for 2D simulations and a few hours for 3D ones on a personal laptop, provided that the numerical model is not optimized.

3.1.2 Simulation of the blocks propagation

In total, the simulation of block propagation requires the definition of the terrain, as a triangulated surface or a polyline, of the block geometry, as a meshed polyhedron or polygon, of the soil properties at all points of the site, by means of three parameters (e_c , μ_c, $\mu_{r,c}$), and of the initial release conditions (block location and orientation).

The block size, global shape (characterized by the three dimensions of the minimal parallelepiped including the block), and initial release conditions (initial location and orientation) can be either defined as **a)** single values, if a specific unstable rock compartment is identified, or **b)** variables quantities, if different block sizes, shapes and initial release conditions, have been identified in a field survey. It is also possible to set the initial block velocity at a non-null value, as sometimes done in propagation models to reproduce specific release conditions. However, in this paper, block velocity is set at nil value in accordance with the experimental procedure.

Global homogeneous zones in the site are defined and associated with different soil properties, i.e. with deterministic values of e_c , μ_c, $\mu_{r,c}$. We assume that the variability of the soil properties in a homogeneous zone is a relatively minor cause of block trajectory variability.

Finally, the detailed block shape and initial orientation are randomly set for each block release, assuming that these quantities are the main causes of the variability of the block propagation process.

3.2 Simulations of the experiments

For the 3D simulations of the experiments, a $1m$ resolution DTM was built from the resampling of the $0.2m$ resolution DTM generated. The decrease in DTM resolution is required because, as the model of the interaction between the block and the soil does not explicitly integrate soil plastic strains, a $0.2m$ resolution DTM would model local topography details that are suppressed in real impacts due to cratering. One can note that the decrease in DTM resolution also drastically decreases computational time.

Profiles starting from the release zones were extracted from the $1m$ DTM for the 2D simulations. The profiles were chosen from expert assessment of the main propagation corridors. For path A, the profile was generated along the steepest slope direction. For path B, a profile passing through the upper corridor, bordered by a rock cut and a talus, and following the steepest slope direction down this

corridor was built. At the crossing with the tracks, the profile crosses the track following the steepest slope direction of the above slope.

Each block propagation simulation set corresponds to the simulation of n block propagations. For each propagation simulation set, the stopping points of all blocks were stored as well as the velocities and heights of the blocks passing through the ES.

For each block propagation, a set of four block properties (three block dimensions L_1, L_2, L_3, and the block mass m_b) was sampled among the quantities measured in the experiments. In 3D, a convex irregular polyhedron was generated so as to fit into a parallelepiped of dimensions L_1, L_2, L_3. Similarly, a convex irregular polygon fitting into a rectangle was generated in 2D. The choice of the size of the rectangle, from the three block dimensions, is potentially crucial. Preliminary simulations showed that, as the experimental blocks were globally compact (Bourrier et al., 2020) according to Sneed and Folk's classification (Sneed and Folk, 1958), i.e. with similar values for the three dimensions, this choice did not affect the simulations significantly enough to analyze the influence of this assumption. Consequently, we arbitrarily choose the dimensions L_1 and L_2.

The polyhedron, or polygon, generation procedure consists of generating a point cloud, then identifying the points bordering the point cloud and, finally, creating a convex envelope using these points (triangulated surface in 3D or polyline in 2D). The mass of the measured block is assigned to the body generated.The number of points of the convex envelope impacts the shape of the polyhedron or polygon. The shape of the convex polygons was controlled by means of the number of points of the initial point cloud used to generate the convex polygonal envelope: the larger the number of points in the point cloud, the larger the number of segments of the polygon. In the absence of experimental measurments of block shape, we set the parameters of the generation algorithm so that the mean number of points of the convex envelope was around 50 in 3D and 20 in 2D. Given the arbitrary character of the block shape generation procedure, we performed additional analysis of the effect of block shape in 2D (see section 4.2). For these simulations, two other types of irregular polygon, with smaller (10 points - called *Sharp polygon*) and larger (40 points - called *Round polygon*) numbers of points of the convex envelope, were used. In addition, rectangular blocks and EOTA (rectangles with "cut corners") blocks (EOTA, 2018) with the same slenderness as the experimental blocks were modelled.

The horizontal initial coordinates of the blocks were randomly chosen within ranges of values corresponding to the experiments. The initial vertical location of the block was defined so that the initial height of the block gravity center above the slope surface was equal to $4m$ for path A, or $2m$ for path B. Finally, the orientation

was randomly set using one random unit quaternion in 3D or one random angle in 2D. Although some block propagation models allow the initial velocity to be set at a non-null value, we initialized block velocity at nil value, in accordance with the experimental procedure.

Homogeneous zones in terms of soil properties (Fig. 3) were determined by expert knowledge with the objective of limiting the different types of soils. Assuming that the subvertical rock cuts are not impacted by blocks, only two different soil types were defined in the site: loose quarry waste, mixing sand, clay, and limestone fragments, encountered in slope zones, and compact quarry waste, corresponding to the tracks and terminal deposit areas. Fixed values of the three parameters associated with soil properties were set for each soil type.

Finally, for each simulation set (Fig. 4), the only physical unknown parameters are the soil properties that are set to match the results (calibration phase) or according to previous results (validation phase).

4 Calibration and assessment of the block propagation model

The approach proposed is based on a practice-oriented calibration procedure. To limit the computational and field measurement efforts, we choose to use the 2D propagation model for the calibration, taking the risk that the values of parameters obtained from this calibration may not be suitable for 3D block propagation models. Indeed, 2D models limit the possible trajectories to a 2D profile. They also entail substantial assumptions in terms of block shape, interaction with the slope surface, and block behavior during the flight phase.

The experimental dataset available is well adapted to evaluate the relevance of this approach since the substantial amount of data on two different propagation paths having the same soil types allows the use of different data for the calibration of the model and for the assessment of its predictive capabilities. To this end, only the experimental data on path A were used for the calibration of the soil properties using 2D simulations so that the experimental results obtained for path B could be dedicated to validation only.

The experimental results available for both paths correspond to the propagation of approximately fifty blocks along each path. We choose to perform calibration using simulation sets of $n = 50$ block releases to compare samples of the same size as in the experiments and to limit the simulation duration. As this limited amount of block release is probably not sufficient to assess the complete variability of the block propagation, we additionally compared different simulation results obtained with $n = 50$ among each other and with results obtained for increasing numbers of block releases.

We used both the measurements of the stopping points and of the velocities for the comparisons between the experiments and the simulations. In 2D, the locations of the stopping points cannot directly be used for such a comparison as the blocks do not necessarily propagate through the profiles chosen for the simulations. For that reason, instead of comparing the stopping distances, we compared the percentages of blocks located in experimentally identified preferential deposit zones (Fig. 5).

In the following, the calibration that allows the determination of the optimal soil properties is presented first. Then, the applicability and the robustness of the simulations are investigated. The repeatability of the simulation results and the influence of the number n of block propagations per simulation set were used to assess the applicability while the analyses of the influence of the modeling of blocks shape and of soil properties allowed the evaluation of the model robustness.

4.1 Calibration using 2D simulations

The calibration phase consisted of iteratively selecting the values of the soil properties that lead to the best match between the simulation and the experimental results. Although a more complex calibration procedure, based on optimization processes for example (Mollon et al., 2012), could have been more efficient, we chose a calibration procedure corresponding to the classical use of block propagation models by practitioners.

The first step of the calibration consisted of setting values of the soil properties for Soil 1 (Fig. 3) that reproduce the experimental trajectories of the block along the uphill slope. In this part of the slope, the blocks propagated by successions of very small rebounds which induced low velocities, ranging between almost nil ones and $7.5 m/s$ (Fig. 6), at $ES1 - A$. Very few blocks were stopped in this part of the slope: 2% of the blocks were stopped in zone 1A and 2% in zone 2A.

The setting of parameters for Soil 1 is challenging because it requires finding sets of values that allow propagation of the block at low velocity until $ES1 - A$ and very few blocks stop in zones $1A$ and $2A$. The best fit parameters (Table 1) result in very few block stops and similar velocity ranges to the experiments at $ES1 - A$ (Fig. 6). However, the parameters chosen entail slight overestimation of the block stopping in zones $1A$ and $2A$. In addition, even if the velocity ranges are similar, we did not manage to find parameters that reproduce the experimental velocity distribution at $ES1 - A$, in particular the large number of blocks with small velocities. Consequently, the propagation of a large number of blocks with small velocities at $ES1 - A$ seems not to be possible using this model.

Despite these differences, the parameter set chosen remains the most suitable obtained from calibration. Other sets of parameters either yielded too many blocks stopped before $ES1 - A$ or too high velocities at $ES1 - A$.

The direct setting of parameters associated with Soil 2 at the same values as for Soil 1 (Fig. 6 - 1 zone) provides simulation results that match well with experimental results in terms of velocity ranges at $ES2 - A$ and of relative distributions between the blocks stopped in zones $3A$ and $4A$. The predictions of both quantities were improved (Fig. 6 - 2 zones) considering that Soil 2 leads to more frictional dissipation (Table 1), i.e. larger values of both μ_c and $\mu_{r,c}$, since it is more compact.

In an attempt to improve the predictions of block propagation in the upper part of the slope, a third zone, corresponding to the release zone of the blocks (Fig. 1) was defined. $\mu_{r,c}$ was set at nil value in this zone to favor initial propagation of the blocks (Fig. 6 - 3 zones). This change slightly improved the distribution of block stopping points, since a smaller number of blocks were stopped in zones $1A$ and $2A$, but it did not improve the quality of the calibration in terms of matching the experimental distribution of the velocities at $ES1 - A$.

It is worth noting that the calibration of the soil properties (Table 1) finally lead to setting the restitution coefficient e_c at nil value for both soils. This setting is in accordance with two qualitative experimental observations: i) the blocks do not bounce when vertically impacting horizontal surfaces, ii) the velocity of the impact point normal to the impacted surface seems very small compared to the tangential one.

One can also note that the differences between the two latter simulations for zones $1A$ and $2A$ as well as for $ES1 - A$ illustrate the fact that using $n = 50$ is not sufficient for a complete assessment of the variability of the simulation results due to different initial block shapes and orientations.

4.2 Relevance and robustness of the simulations

The comparison between different simulation sets for $n = 50$ (Fig. 7) allow the quantification of the variability associated with these simulations. The results obtained show that the different simulations are qualitatively similar in terms of relative number of blocks stopped in the different zones and of velocity ranges at $ES1 - A$ and $ES2 - A$. However, significant quantitative differences between the simulation sets exist both in terms of percentages of blocks stopped in the different zones and velocity distributions at ES.

The differences between the results tend to decrease, both in terms of stopping points and velocities, for increasing values of n (Fig. 8). However, even between

large numbers of block releases ($n = 500$ and $n = 2000$, for example), some differences remain. However, the smaller sample ($n = 50$) is a good indicator of the general trends of the simulations for larger values of n. Consequently, simulation sets with $n = 50$ were considered sufficient to provide representative numerical results.

Under the simulation assumptions described in section 3.2, the simulation parameters that can influence the results are the initial orientation, the block shape and the soil properties. While the influence of the initial orientation was explored by making n block releases, the influence of the two latter parameters was analysed by comparing with the variability between the simulation sets for $n = 50$ (Fig. 7).

Simulations with the best fit soil properties (Table 1) and different block shapes have been performed. Rectangular blocks, EOTA (rectangles with "cut corners") blocks (EOTA, 2018), and two convex polygons, made of smaller (*Sharp polygon*) and larger (*Round polygon*) numbers of segments, were modelled. These simulations (Fig. 9) showed that the influence of block shape is significantly larger than the variability observed for $n = 50$ (Fig. 7) only for cubes and EOTA blocks. On the contrary, the shape of the random polygons exhibits influences of the same order of magnitude as the variability observed for $n = 50$. These results show that the influence of block shape modeling is important. In particular, the use of irregular polygons instead of regular shapes entails substantial differences. The assumptions of block shape modeling should thus be chosen cautiously.

The influence of soil properties was explored using constant soil properties on the study site and irregular block shapes with mean number of points of the convex envelope set at 20. In this analysis, initial values of the soil parameters were first defined. The restitution coefficient e_c was set at nil value, the friction coefficient was set $\mu_c = 0.6$, and the rolling friction coefficient $\mu_{r,c}$ was set at nil value. The influence of each soil parameter was explored by varying each individually in turn.

The results obtained show significant influence of e_c (Fig. 11) and $\mu_{r,c}$ (Fig. 12) compared with differences in simulation sets for $n = 50$ (Fig. 7), whereas the influence of μ_c (Fig. 10) remains of the same order of magnitude as the variability observed for $n = 50$. These results show that the calibration of the parameters should focus on the choice of e_c and $\mu_{r,c}$ since these parameters have a major influence. On the contrary, the setting of μ_c is less crucial. One can also note that the increase in the velocities at $ES1-A$ for increasing values of e_c tends to confirm the relevance of choosing almost nil values of e_c.

As for the influence of block shape, the influence of soil parameters can be explained from a physical point of view. Increases in e_c and decreases in $\mu_{r,c}$ entail less energy dissipation and, consequently, more propagation and larger velocities. The influence of μ_c is more complex to interpret since the influence of this param-

eter is less significant. $\mu_c = 0.6$ seems to be in the vicinity of a threshold value. For $\mu_c = 0.4$, the blocks propagate preferentially by sliding with small frictional dissipation and thus travel further than for $\mu_c = 0.6$. For $\mu_c = 0.8$, the blocks tend to more preferentially roll and thus also propagate further than for $\mu_c = 0.6$.

4.3 Predictive capabilities of the block propagation model

The soil parameters calibrated in 2D using the experimental results on path A (Table 1) have been used in 2D simulations to predict block propagation on path B. The predictions obtained provide relevant information concerning the preferential deposit zones, the mean velocities at $ES1 - B$ and the velocity range at $ES2 - B$ (Fig. 13). However, the percentages of blocks stopped are underestimated for zone $1B$ and $3B$ and overestimated for zones $2B$ and $4B$. The extremely low and high values of velocities at $ES1 - B$ are also not predicted. Finally, the details of velocity distribution at $ES2 - B$ are not predicted. One can note that the variability of the results for different simulation sets is of the same order as for path A. Consequently, the soil parameters calibrated for path A provide the same level of accuracy in terms of block propagation prediction for path B.

The use of 3D simulations to predict block propagation on path B using soil parameters calibrated in 2D on path A improves the quality of the predictions (Fig. 14) in terms of velocity distribution prediction and relative order of the preferential deposit zones. Quantitatively, the same differences as for 2D simulations are observed. This result illustrates the fact that the parameters calibrated using a 2D model can provide the same level of accuracy when used to model block propagation in 3D in another propagation path.

Interestingly, simulations of block propagation in 3D on path A (Fig. 15) using the same soil properties as in 2D provide slightly better results in terms of velocity distribution prediction. However, the limitation concerning too many blocks stopping in the uphill part of the site remains.

Finally, the distribution of the block stopping points obtained from 3D simulations (Fig. 16) on path A exhibit similar lateral dispersion as in the experiments. As observed in Fig. 15, a significant over-representation of blocks are stopped on the uphill slope. For path B, although too many blocks are stopped on the uphill track compared to the ones stopped on the downhill one, the simulations predict well the substantial 3D deviations of the blocks from the main corridor.

5 Conclusion

The model proposed is based on a rigorous mechanical and numerical modeling of block propagation that focuses on the main parameters influencing the propagation. The model allows the integration of the effects of topography, block shape, initial location and orientation in a detailed manner and a contact model is integrated to reproduce the interaction between the soil and block. The contact model, based on sound mechanical bases, involves a limited number of parameters related with the main physical process. The restitution coefficient quantifies soil plasticity, viscosity and mechanical wave propagation, the friction at the interface is also implemented as well as a Coulomb-type rolling friction process which models cratering and resistance of the soil to block rolling around the contact point. In total, only three parameters are required to define soil properties in terms of interaction with the block.

The modeling approach proposed is among the more complex and detailed ones in trajectory analyses. The model belongs to the class of "rigid body" models which are classically identified as more complex than "lumped mass" ones (Volkwein et al., 2011). Compared to "lumped mass" models, "rigid body" models are based on more advanced mechanical concepts. In particular, instead of considering the block as a material point and using rebound models involving changes of the block velocities at its center of gravity only, they explicitly model the block shape and the interaction at the contact scale. This increased complexity does not necessarily entail increases in the number of parameters and simplifies the physical interpretation of the results. Among the propagation models explicitly integrating block shape, the model proposed is based on nonsmooth mechanics which allows a modeling of the contact as an interaction between perfectly rigid bodies. All the dissipation processes are modeled in the interface, keeping the intrinsic sticking feature of friction. In standard discrete element methods, Coulomb friction is generally regularized leading to non realistic viscous friction when sticking. The approach proposed in this paper does not require the introduction of local compliance at the contact scale which is usually difficult to measure experimentally, does not introduce damping, and allows the use of a more diversified range of numerical solving schemes. In particular, the numerical scheme used in this study allows the avoidance of artificial viscosity. Typically, artificial viscosity is added to ensure the numerical stability of the scheme, but results in unrealistic energy balances. The specificity of the modeling approach proposed will be crucial for several modeling improvements envisaged such as, for instance, coupling with other mechanical models (e.g. models of protection structures) or the modeling of block fragmentation during propagation. One can note that most of the model-

ing features presented in this paper are freely available in the open-source block propagation models platform Platrock[2] and its coupling with Siconos.

In addition, the simulation procedure proposed as well as the results obtained in terms of calibration of the models and assessment of their predictive capabilities constitute original outcomes of interest for the assessment of block propagation simulation quality.

The simulation procedure proposed allows the modeler to explicitly set the parameters that can be assessed in the field while the variability of the parameters that cannot be estimated (block shape and initial orientation, in this study) is explored statistically. This principle favors the practical usefulness of the procedure for practicing engineers. In the context of this study, the parameters set by the modeler were the global block properties (mass and sizes), the topography, and the release zone location, including the release height. The soil properties are also modeler-defined parameters but they are more difficult to set since they cannot directly be measured. In this study, they were calibrated and then used as input parameters to assess the predictive capabilities of the model.

A classical calibration procedure based on setting of the soil properties by trial and error was chosen in accordance with the engineering practices in the field of trajectory analysis. As this calibration uses 2D propagation models, it is feasible for use in engineering practice, given the computational efficiency of 2D models. To complement this point, the use of calibration data at the field scale, of block stopping points locations in particular, highlights the applicability of the procedure proposed since the latter data is more easily accessible to practitioners, compared to data at the rebound scale in particular. Finally, this study presents a calibration method based on comparisons with the complete distributions of several experimental measurements, and not only to global indicators (such as mean or maximum values) of these distributions, which is not typical in the literature.

The principle of the practice-oriented calibration procedure proposed was to use a 2D propagation model for the calibration to limit the computational and field measurement efforts, taking the risk that the values of parameters obtained from this calibration may not be suitable for 3D block propagation models. The propagation simulations obtained in 2D and 3D, performed with the parameters calibrated in 2D, exhibit the same level match to the experimental results. Consequently, the proposed procedure is appropriate for an optimal parameter calibration. One can note that extensive Monte-Carlo 3D simulations, potentially using a coarser DTM, can constitute an alternative to such an optimal calibration procedure provided that sufficient computational resources are available.

---

[2] https://gitlab.com/platrock/platrock

As is classically the case in trajectory analyses, the calibrated model simulations predict the main characteristics of the propagation, that is the preferential deposit zones and the range of velocities at specific locations, but not the quantitative details of the stopping points and velocity distributions. In particular, significant differences are observed with regards to the detailed distribution of the velocities and block stopping points. The simulations performed with the calibrated model on path B show the capacity of the model to predict the main characteristics of the propagation on path B. The level of experimental match is of the same order as in the calibration phase, i.e. for 2D simulations on path A. The similar level of experimental match in the calibration and validation phases highlights that rebound model parameters can be associated with soil types, at least on this example. This generic feature of the model setting is crucial in terms of industrial applicability since, after a calibration phase on a sufficient number of soil types, the model may be used in a predictive manner.

Although the results obtained in this specific context are promising, the modeling and calibration approaches still have to be adapted for a practical use since the conditions of the field experiments presented do not fully correspond to typical practical conditions. In practice, the block release point, volume, shape and orientation are not fixed. They have to be assessed from field observations and, in most cases, release point locations and volumes have to be explored statistically in addition to block shape and orientation. In addition, in the absence of an exhaustive calibration of the model for a large range of soil types, additional calibrations will have to be performed which is a difficult task mainly because of the questions of the number and of type of data required for a correct calibration.

The results presented in this paper exhibit a level of experimental match that may not look sufficient for a quantitative design of protection structures or for precise hazard zone delineation. However, the results tend to show that the deficiencies are more in the details of the velocity distribution than in the global range of velocities. Consequently, it may be possible to design a structure on the basis of the predicted extreme quantities. In the same vein, differences in terms of block stopping points are mainly observed for small and medium propagation distances which is of smaller importance in practice than the blocks that demonstrate large propagation distances. In addition, the level of experimental match, although rather small, can be complemented with uncertainty assessment to provide additional information that will increase awareness in the process of design or hard zone delineation.

6 Conclusion

References

Acary V (2015) Energy conservation and dissipation properties of time-integration methods for the nonsmooth elastodynamics with contact Article published online

Acary V, Bourrier F (2021) Coulomb friction with rolling resistance as a cone complementarity problem. European Journal of Mechanics, A/Solids 85, DOI 10.1016/j.euromechsol.2020.104046

Acary V, Brogliato B (2008) Numerical methods for nonsmooth dynamical systems. Applications in mechanics and electronics. Lecture Notes in Applied and Computational Mechanics 35. Berlin: Springer. xxi, 525 p.

Acary V, Brémond M, Huber O (2018) Advanced Topics in Nonsmooth Dynamics., Acary, V. and Brüls. O. and Leine, R. (eds). Springer Verlag, chap On solving frictional contact problems: formulations and comparisons of numerical methods.

Acary V, Bonnefon O, Brémond M, Huber O, Pérignon F, Sinclair S (2019) An introduction to Siconos. Technical Report RT-0340, INRIA, URL https://hal.inria.fr/inria-00162911

Asteriou P, Tsiambaos G (2018) Effect of impact velocity, block mass and hardness on the coefficients of restitution for rockfall analysis. International Journal of Rock Mechanics and Mining Sciences 106:41 – 50, DOI https://doi.org/10.1016/j.ijrmms.2018.04.001

Bourrier F, Hungr O (2013) Rockfall Engineering, ISTE-Wiley, chap Rockfall Dynamics: A Critical Review of Collision and Rebound Models, pp 175–209. DOI 10.1002/9781118601532.ch6

Bourrier F, Berger F, Tardif P, Dorren L, Hungr O (2012) Rockfall rebound: comparison of detailed field experiments and alternative modelling approaches. Earth Surface Processes and Landforms 37(6):656–665, DOI 10.1002/esp.3202

Bourrier F, Toe D, Garcia B, Baroth J, Lambert S (2020) Experimental investigations on complex block propagation for the assessment of propagation models quality. Landslides DOI 10.1007/s10346-020-01469-5

Brogliato B (2016) Nonsmooth Mechanics: Models, Dynamics and Control, 3rd edn. Communications and Control Engineering, Springer-Verlag, London

Caviezel A, Demmel SE, Ringenbach A, Bühler Y, Lu G, Christen M, Dinneen CE, Eberhard LA, von Rickenbach D, Bartelt P (2019) Reconstruction of four-dimensional rockfall trajectories using remote sensing and rock-based accelerometers and gyroscopes. Earth Surface Dynamics 7(1):199–210, DOI 10.5194/esurf-7-199-2019

Crosta G, Agliardi F (2004) Parametric evaluation of 3D dispersion of rockfall trajectories. Natural Hazards and Earth System Sciences 4:583–598

Descoeudres F, Zimmermann T (1987) Three-dimensional dynamic calculation of rockfalls. In: Proceedings of the 6th International Congress on Rock Mechanics - Montreal, Balkema, Rotterdam, pp 337–342

Dorren L (2003) A review of rockfall mechanics and modelling approaches. Progress in Physical Geography 27(1):69–87, DOI 10.1191/0309133303pp359ra

Dorren L, Berger F, Putters U (2006) Real-size experiments and 3D simulation of rockfall on forested and non-forested slopes. Natural Hazards and Earth System Sciences 6(1):145–153

EOTA (2018) Falling rock protections kits. ead 340059-00-0106/c 417/07. technical report

Falcetta, JL (1985) Un nouveau modèle de calcul de trajectoires de blocs rocheux. Rev Fr Geotech (30):11–17, DOI 10.1051/geotech/1985030011, URL https://doi.org/10.1051/geotech/1985030011

Garcia B, Richefeu V, Baroth J, Daudon D, Villard P (2020) Collision of shaped boulders with sand substrate investigated by experimental, stochastic, and discrete approaches. Journal of Geophysical Research: Earth Surface 125(11), DOI 10.1029/2019JF005500

Géradin M, Cardona A (2001) Flexible Multibody Dynamics: A finite element Approach. J. Wiley & Sons, New York, 340 p.

Giani GP, Giacomini A, Migliazza M, Segalini A (2004) Experimental and theoretical studies to improve rock fall analysis and protection work design. Rock Mechanics and Rock Engineering 37(5):369–389, DOI 10.1007/s00603-004-0027-2

Guzzetti F, Crosta G, Detti R, Agliardi F (2002) Stone: a computer program for the three-dimensional simulation of rock-falls. Computer and Geosciences 28:1079–1093

Hu J, Li S, Li L, Shi S, Zhou Z, Liu H, He P (2017) Field, experimental, and numerical investigation of a rockfall above a tunnel portal in southwestern china. Bulletin of Engineering Geology and the Environment DOI 10.1007/s10064-017-1152-y

Jean M, Moreau J (1987) Dynamics in the presence of unilateral contacts and dry friction: a numerical approach. In: Del Pietro G, Maceri F (eds) Unilateral

problems in structural analysis. II, CISM 304, Spinger Verlag, pp 151–196

Jourdan F, Alart P, Jean M (1998) A Gauss Seidel like algorithm to solve frictional contact problems 155(1):31–47

Koo C, Chern J (1998) Modification of the dda method for rigid block problems. International Journal of Rock Mechanics and Mining Sciences 35(6):683–693

Labiouse V, Heidenreich B (2009) Half-scale experimental study of rockfall impacts on sandy slopes. Natural Hazards and Earth System Sciences 9(6):1981–1993, DOI 10.5194/nhess-9-1981-2009

Lan H, Derek Martin C, Lim C (2007) Rockfall analyst: A GIS extension for three-dimensional and spatially distributed rockfall hazard modeling. Computers and Geosciences 33(2):262–279

Leine RI, Schweizer A, Christen M, Glover J, Bartelt P, Gerber W (2014) Simulation of rockfall trajectories with consideration of rock shape. Multibody System Dynamics 32(2):241–271, DOI 10.1007/s11044-013-9393-4

Lu G, Caviezel A, Christen M, Demmel S, Ringenbach A, Bhler Y, Dinneen C, Gerber W, Bartelt P (2019) Modelling rockfall impact with scarring in compactable soils. Landslides 16(12):2353–2367, DOI 10.1007/s10346-019-01238-z

Lu G, Ringenbach A, Caviezel A, Sanchez M, Christen M, Bartelt P (2020) Mitigation effects of trees on rockfall hazards: does rock shape matter? Landslides DOI 10.1007/s10346-020-01418-2

Mollon G, Richefeu V, Villard P, Daudon D (2012) Numerical simulation of rock avalanches: Influence of a local dissipative contact model on the collective behavior of granular flows. Journal of Geophysical Research: Earth Surface 117(2), DOI 10.1029/2011JF002202

Moreau J (1988) Unilateral contact and dry friction in finite freedom dynamics. In: Moreau J, PD P (eds) Nonsmooth Mechanics and Applications, CISM 302, Spinger Verlag, pp 1–82

Sneed ED, Folk RL (1958) Pebbles in the Lower Colorado River, Texas a Study in Particle Morphogenesis. Journal of Geology 66:114–150, DOI 10.1086/626490

Spadari M, Giacomini A, Buzzi O, Fityus S, Giani G (2012) In situ rockfall testing in new south wales, australia. International Journal of Rock Mechanics and Mining Sciences 49:84 – 93, DOI https://doi.org/10.1016/j.ijrmms.2011.11.013

Toe D, Bourrier F, Dorren L, Berger F (2018) A novel dem approach to simulate block propagation on forested slopes. Rock Mechanics and Rock Engineering 51(3):811–825, DOI 10.1007/s00603-017-1348-2

Volkwein A, Schellenberg K, Labiouse V, Agliardi F, Berger F, Bourrier F, Dorren L, Gerber W, Jaboyedoff M (2011) Rockfall characterisation and structural protection - a review. Natural Hazards and Earth System Science 11(9):2617–2651, DOI 10.5194/nhess-11-2617-2011

Volkwein A, Brgger L, Gees F, Gerber W, Krummenacher B, Kummer P, Lardon J, Sutter T (2018) Repetitive rockfall trajectory testing. Geosciences (Switzerland) 8(3), DOI 10.3390/geosciences8030088

Williams C, Morkeh J, Dorfschmidt K, Poon C, Matlashewski P, Carvalho J (2020) Innovative rockfall solutions based on calibration and field testing. Mining, Metallurgy and Exploration 37(1):101–116, DOI 10.1007/s42461-019-0092-4

Yan P, Zhang J, Kong X, Fang Q (2020) Numerical simulation of rockfall trajectory with consideration of arbitrary shapes of falling rocks and terrain. Computers and Geotechnics 122, DOI 10.1016/j.compgeo.2020.103511

	Soil 1	Soil 2
e_c	0.	0.
μ_c	0.5	0.6
$\mu_{r,c}$ (m)	0.04	0.05

Table 1: Soil properties obtained from calibration
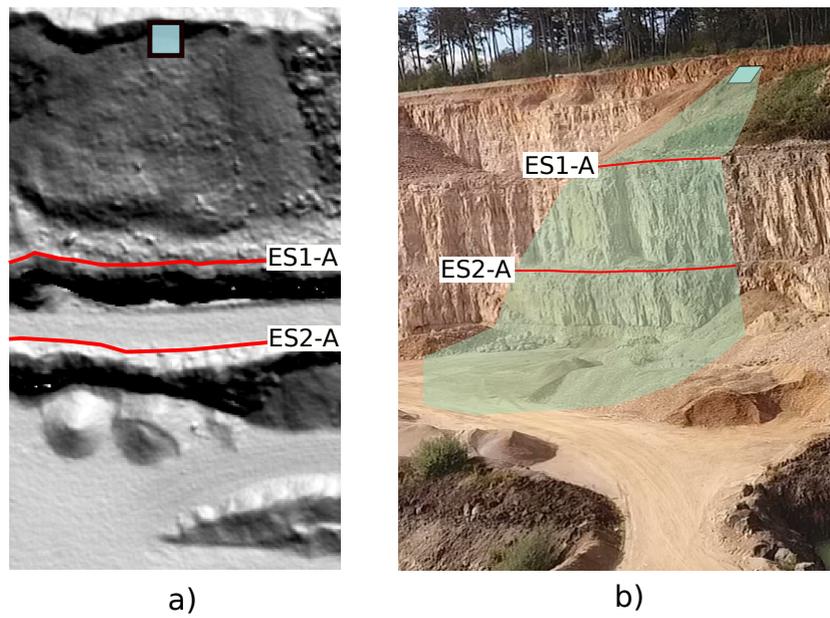
Fig. 1: Overview of path A (a: topview of a hillshade built from a 1m resolution DTM, b: general view) including the location of the Evaluation Screens ($ES1 - A$ and $ES2 - A$), of the release zone (green square), and of the potential propagation zone (light green zone).

a)   b)
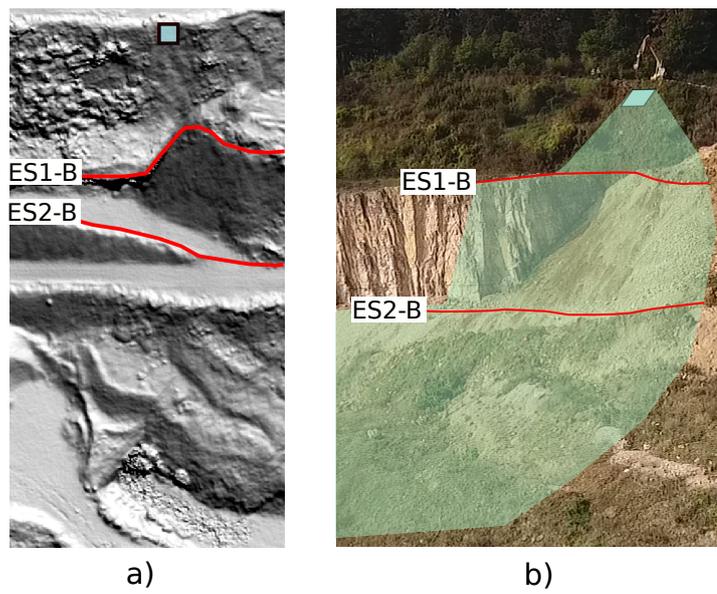
Fig. 2: Overview of path B (a: topview of a hillshade built from a 1m resolution DTM, b: general view) including the location of the Evaluation Screens ($ES1-B$ and $ES2-B$), of the release zone (green square), and of the potential propagation zone (light green zone).
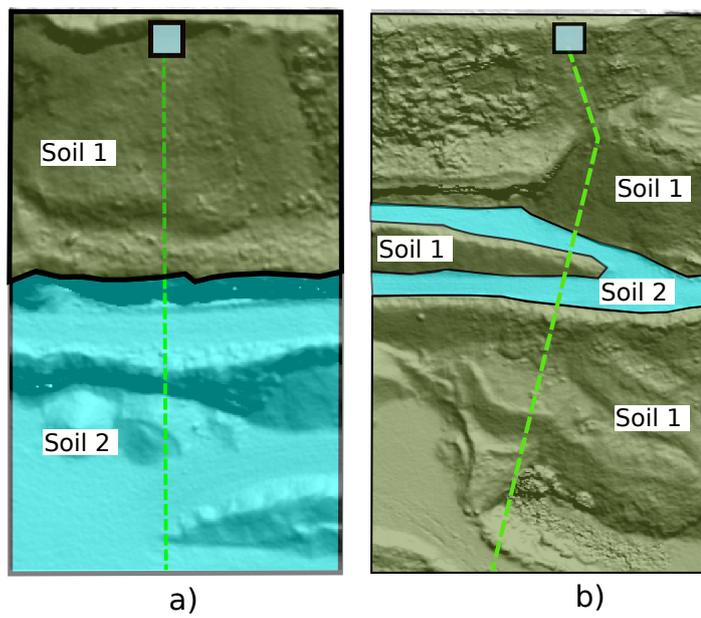
Fig. 3: Homogeneous zones in terms of soil properties determined by expert knowledge on the propagation paths A (a) and B (b). Two different soil types were defined at the site.
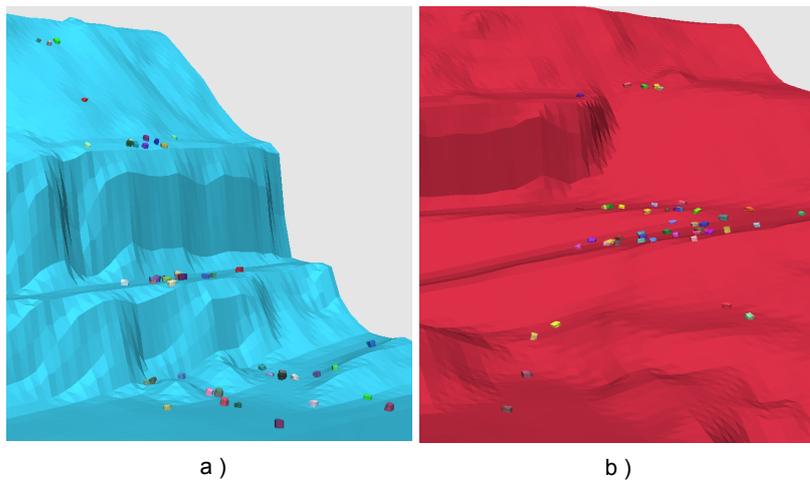
Fig. 4: Examples of block stopping points obtained from propagation simulations on path A (a) and path B (b).
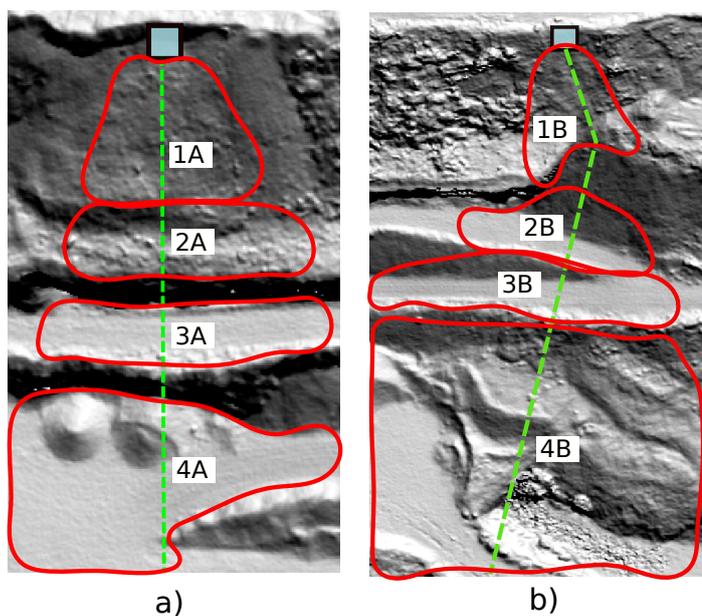
Fig. 5: Preferential deposit zones identified during the experimental campaign for path A (a) and path B (b) (Bourrier et al., 2020).
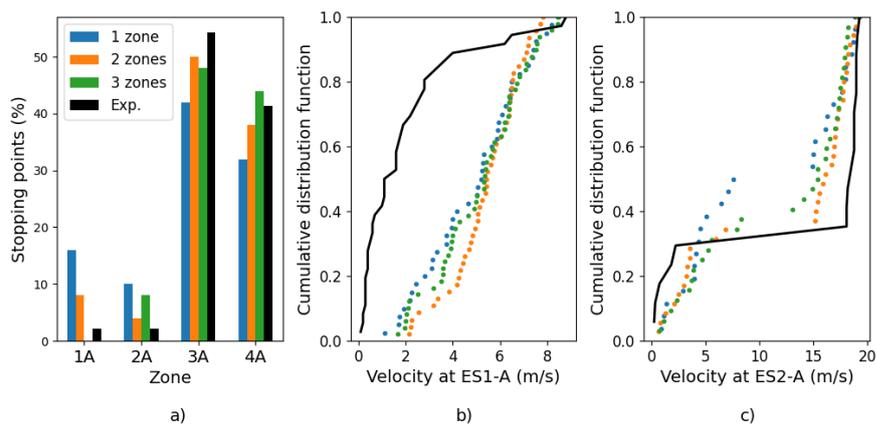
Fig. 6: Comparison between experiments and simulations results obtained for path A using the soil parameters associated with Soil 1 along the complete path (1 zone), or the best fit parameters for Soil 1 and 2 (2 zones), or the best fit parameters for Soil 1 and 2 and $\mu_{r,c} = 0$ in the release zone of the blocks (a: distribution of the stopping points between the preferential deposit zones, b: cumulative distribution function of block velocities at $ES1-A$, c: cumulative distribution function of block velocities at $ES2 - A$).
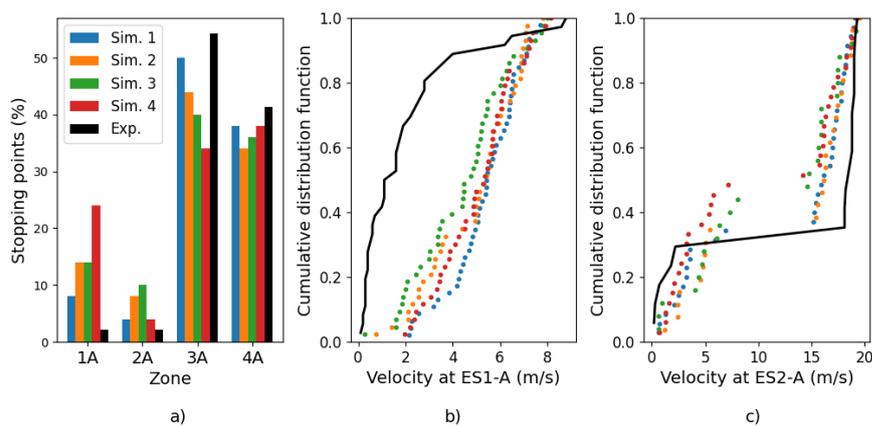
Fig. 7: Results obtained from different simulations of block propagation on path A using the calibrated parameters for soil properties and $n = 50$ (a: distribution of the stopping points between the preferential deposit zones, b: cumulative distribution function of block velocities at $ES1 - A$, c: cumulative distribution function of block velocities at $ES2 - A$).
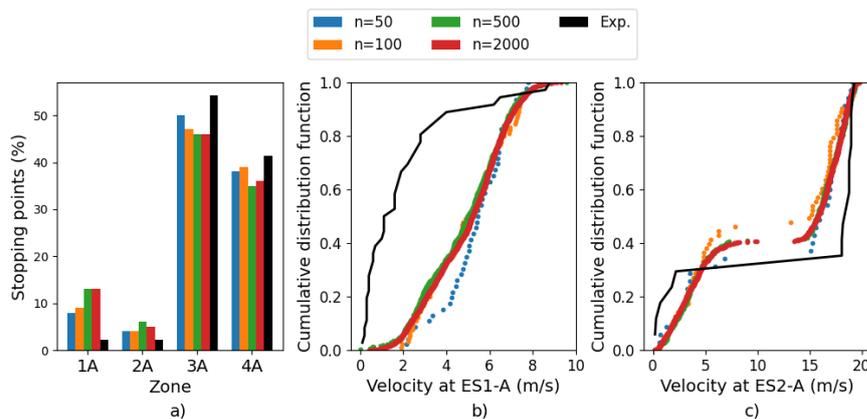

Fig. 8: Results obtained from different simulations of block propagation on path A using the calibrated parameters for soil properties and increasing numbers n of block releases (a: distribution of the stopping points between the preferential deposit zones, b: cumulative distribution function of block velocities at $ES1 - A$, c: cumulative distribution function of block velocities at $ES2 - A$).
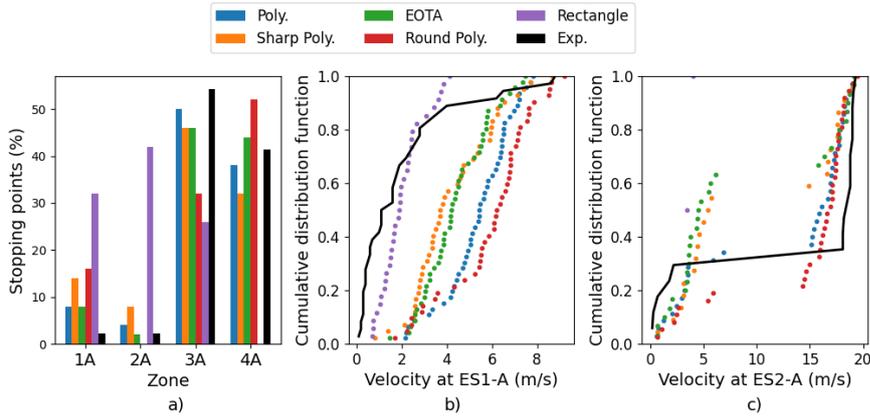
Fig. 9: Results obtained from different simulations of block propagation on path A using the calibrated parameters for soil properties and different block shapes (a: distribution of the stopping points between the preferential deposit zones, b: cumulative distribution function of block velocities at $ES1 - A$, c: cumulative distribution function of block velocities at $ES2 - A$).
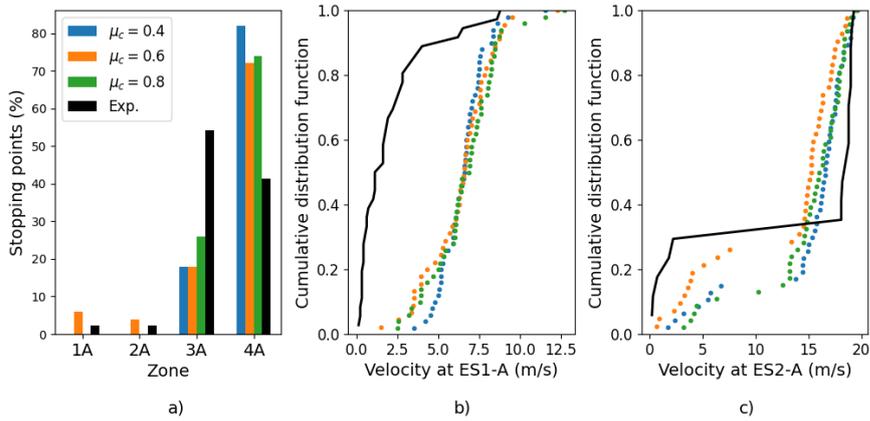
Fig. 10: Results obtained from different simulations of block propagation on path A using $e_c = 0$, $\mu_{r,c} = 0$ and different values of μ_c (a: distribution of the stopping points between the preferential deposit zones, b: cumulative distribution function of block velocities at $ES1-A$, c: cumulative distribution function of block velocities at $ES2 - A$).
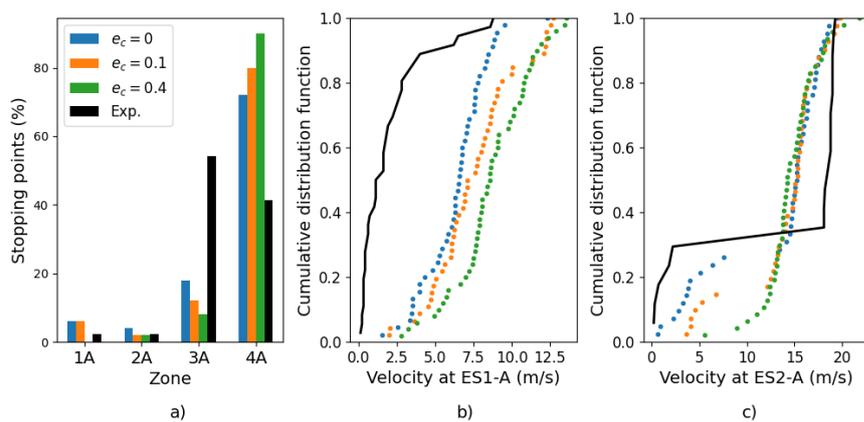
Fig. 11: Results obtained from different simulations of block propagation on path A using $\mu_c = 0.6$, $\mu_{r,c} = 0$ and different values of e_c (a: distribution of the stopping points between the preferential deposit zones, b: cumulative distribution function of block velocities at $ES1-A$, c: cumulative distribution function of block velocities at $ES2 - A$).
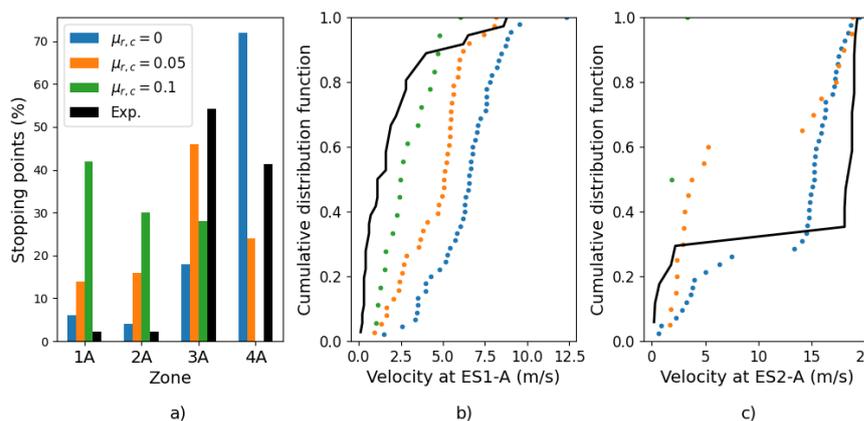
Fig. 12: Results obtained from different simulations of block propagation on path A using $e_c = 0$, $\mu_c = 0.6$ and different values of $\mu_{r,c}$ (a: distribution of the stopping points between the preferential deposit zones, b: cumulative distribution function of block velocities at $ES1-A$, c: cumulative distribution function of block velocities at $ES2 - A$).
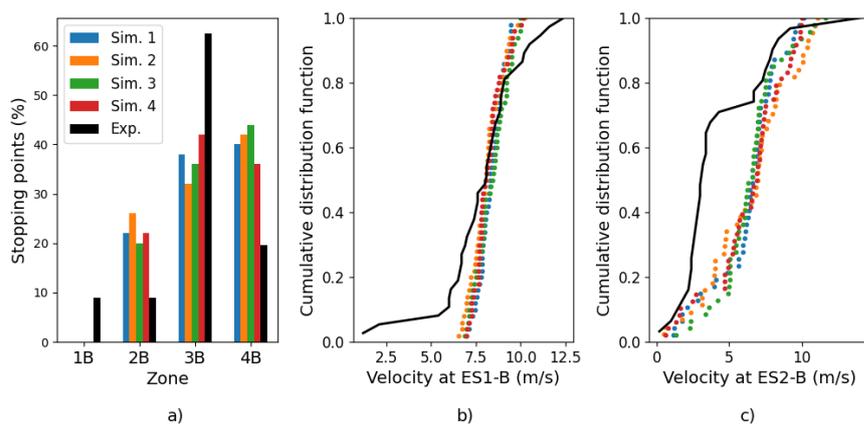
Fig. 13: Predictions of block propagation on path B obtained from 2D simulations with different simulation sets using the calibrated parameters for soil properties and $n = 50$ (a: distribution of the stopping points between the preferential deposit zones, b: cumulative distribution function of block velocities at $ES1 - B$, c: cumulative distribution function of block velocities at $ES2 - B$).
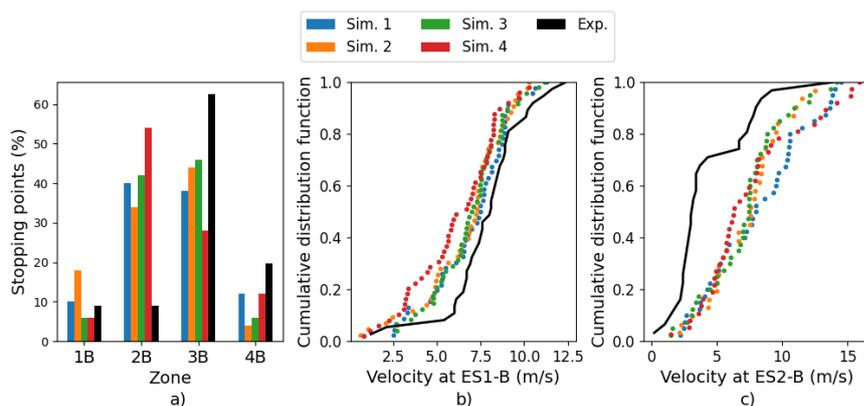

Fig. 14: Predictions of block propagation on path B obtained from 3D simulations with different simulation sets using the calibrated parameters for soil properties and $n = 50$ (a: distribution of the stopping points between the preferential deposit zones, b: cumulative distribution function of block velocities at $ES1 - B$, c: cumulative distribution function of block velocities at $ES2 - B$).
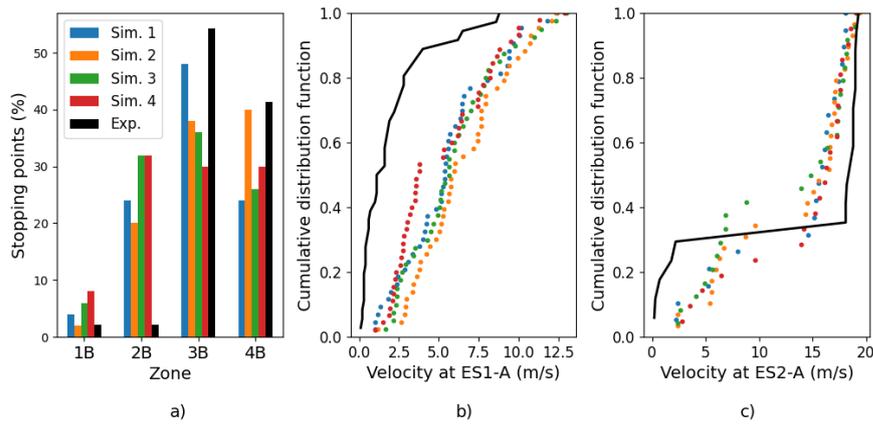
Fig. 15: Predictions of block propagation on path A obtained from 3D simulations with different simulation sets using the calibrated parameters for soil properties and $n = 50$ (a: distribution of the stopping points between the preferential deposit zones, b: cumulative distribution function of block velocities at $ES1 - A$, c: cumulative distribution function of block velocities at $ES2 - A$).
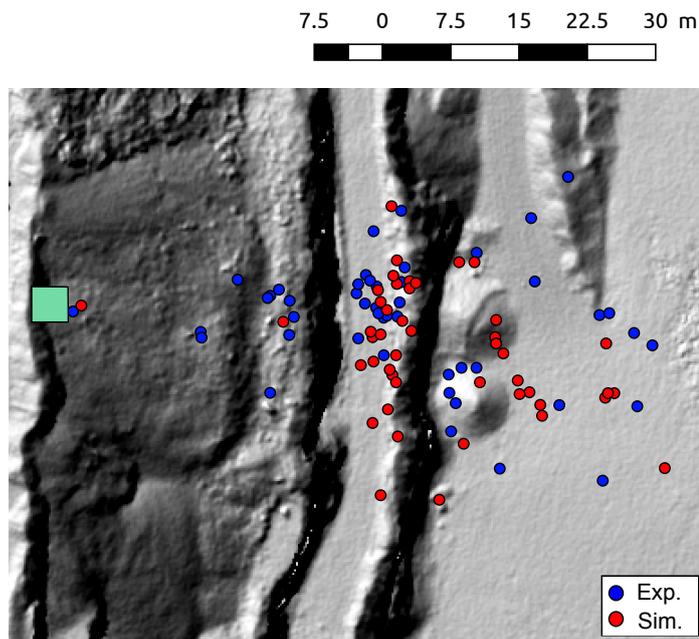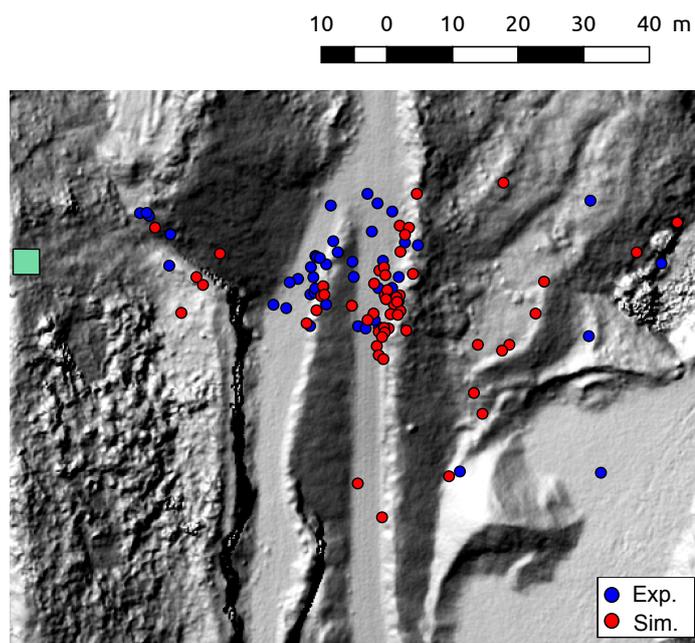
Fig. 16: Predictions of block stopping points on path A (a) and path B (b) obtained from 3D simulations with simulation sets using the calibrated parameters for soil properties and $n = 50$.